ENSO Surface Winds in CCM3 Simulation: Diagnosis of Errors

SUMANT NIGAM AND CHUL CHUNG*

Department of Meteorology, University of Maryland at College Park, College Park, Maryland

(Manuscript received 29 July 1999, in final form 27 October 1999)

ABSTRACT

The structure of surface-wind anomalies associated with ENSO variability is extracted from Comprehensive Ocean–Atmosphere Dataset observations and European Centre for Medium-Range Forecasts (ECMWF) and National Centers for Environmental Prediction (NCEP) reanalyses, along with estimates of uncertainty. The targets are used to evaluate ENSO surface winds produced by the National Center for Atmospheric Research's atmospheric GCM known as the Community Climate Model, version 3 (CCM3), when integrated in the climate-simulation mode. Simulated anomalies have stronger easterlies in the off-equatorial Tropics and stronger equatorward flow in the Pacific than any of the observational estimates do. CCM3's wind departures are found to be large when compared with the difference of the reanalysis anomalies and should thus be considered to be *errors.*

In a companion paper, the authors make a compelling case for the presence of robust errors in CCM3's ENSO heating distribution, based on comparisons with the residually diagnosed heating anomalies from ECMWF and NCEP reanalyses.

The linkage between specific features of CCM3's surface-wind and heating errors is investigated using a steady, linear, global, primitive equation model (18 vertical σ levels, 30 zonal waves, and latitude spacing of 2.5°). Diagnostic modeling indicates that stronger equatorward flow in the Pacific results largely from excessive diabatic cooling in the off-equatorial Tropics, a key heating error linked to a more meridional redistribution of ENSO heating in CCM3. The ''bottom-heavy'' structure of CCM3's equatorial heating anomalies, on the other hand, is implicated in the generation of zonal-wind errors in the central and eastern tropical Pacific.

In the diagnostic simulation of CCM3's ENSO variability, the longwave heating anomalies, with peak values near 850 mb, contribute as much to surface zonal winds as do all other heating components together—a novel finding, needing corroboration.

This study, along with the companion paper, illustrates the dynamical diagnosis strategy—of circulation and forcing intercomparisons with observed counterparts, followed by diagnostic modeling—for analyzing errors in the GCM's simulation of climate variability.

1. Introduction

This analysis was prompted by our interest in using the National Center for Atmospheric Research (NCAR) Climate System Model (CSM[1])—a coupled atmosphere, ocean, land surface, and sea-ice general circulation model (GCM; Boville and Gent 1998)—to study the interaction of Asian summer monsoon and El Niño–Southern Oscillation (ENSO). A preliminary analysis of this interaction was conducted by the authors (Chung and Nigam 1999) using a modified version of a comparatively simpler coupled ocean–atmosphere model (Zebiak and Cane 1987).

The CSM would be an appropriate tool to study monsoon–ENSO interactions, provided it produced a reasonable structure of ENSO (and Asian monsoon) variability. The ocean–atmosphere interannual variability in a 45-year-long CSM integration was analyzed by Meehl and Arblaster (1998). They computed the Southern Oscillation and Niño-3 correlations, and circulation composites during the extremum periods of these indices, and found that ''ENSO-like'' variations in the CSM had substantially different structure in comparison with observations. For example, SST variability in the CSM integration was strongest in the western tropical Pacific, whereas the observed ENSO SST variations are largest in the central and eastern tropical Pacific.[2] Given this discrepancy, the monsoon–ENSO linkage and its un-

* Current affiliation: Center for Clouds, Chemistry, and Climate, Scripps Institution of Oceanography, University of California, San Diego, La Jolla, California.

[1] The CSM structure and performance were described in the June 1998 special issue of the *Journal of Climate.*

Corresponding author address: Sumant Nigam, Room 3403, Computer and Space Sciences Bldg., Dept. of Meteorology, University of Maryland at College Park, College Park, MD 20742-2425.
E-mail: nigam@atmos.umd.edu

[2] ENSO variability is, in fact, monitored using the central and eastern Pacific sector averaged SST: Niño-3.4 (170°–120°W) and Niño-3 (150°–90°W) SST indices, both defined in the 5°S–5°N equatorial belt.

© 2000 American Meteorological Society

Unauthenticated | Downloaded 02/21/24 05:03 PM UTC

derlying mechanism are likely to be somewhat distorted in the CSM. Our interest in CSM thus evolved from one of application to that of investigation.

The objective of the current study is to investigate the reasons for the deficient structure of ENSO-like variability in the CSM integration. The core analysis is concerned with the fulfillment of one of the *necessary* conditions for obtaining realistic interannual variability in coupled ocean–atmosphere model integrations: a high-quality simulation of surface winds by the atmospheric component of CSM when forced by observed SST variations at the lower boundary, that is, in an uncoupled mode. The surface-wind simulation is of special interest in context of ENSO variability because tropical oceans are largely wind driven, which places a premium on having accurate surface-wind simulation before moving into a more interactive modeling environment, such as the CSM's. The atmospheric component of CSM is the Community Climate Model, version 3 (CCM3).

The interannual variability produced in a 45-year-long CCM3 simulation forced by the observed 1950–94 SST has been compared with observations, which include the National Centers for Environmental Prediction (NCEP)–NCAR reanalyses (Kalnay et al. 1996), Xie–Arkin precipitation (Xie and Arkin 1997), and the residually diagnosed diabatic heating (Nigam et al. 2000). Hurrell et al. (1998) found the Southern Oscillation covariant CCM3 rainfall anomalies to be stronger and more widespread over the subtropical subsidence regions but considerably weaker over the tropical subsidence zone in the western Pacific (cf. their Fig. 38). Nigam et al. evaluated CCM3's ENSO heating distribution from intercomparisons with the 3D heating anomalies diagnosed from NCEP and the European Centre for Medium-Range Weather Forecasts (ECMWF) reanalyses. They found the differences between ECMWF and NCEP heating anomalies to be small in comparison with the CCM3 heating departures (from these anomalies), which allowed the characterization of CCM3's ENSO heating: horizontally, as a more meridional redistribution (''Hadley-like''), and vertically, as a substantially ''bottom-heavy'' profile. The former finding is in accord with Hurrell et al.'s (1998) analysis of the Southern Oscillation rainfall anomalies in CCM3.

The structure of ENSO surface winds over tropical oceans in the 45-yr CCM3 simulation has, however, not been documented in earlier studies. The impact of deficiencies in the CCM3's ENSO rainfall and diabatic heating distributions on surface winds also remains to be ascertained, although such analyses would be clearly warranted in understanding the causes of deficient simulation of ENSO variability in the fully coupled CSM integration.

An important goal of this study is also to demonstrate the dynamical diagnosis strategy. In the context of GCM diagnosis, the strategy would begin with quantitative comparisons of the simulated circulation (e.g., tropical surface winds) and its forcing (e.g., diabatic heating) with the observed counterparts—the requisite heating intercomparisons for CCM3 are described in a companion paper [Nigam et al. (2000, this issue), hereinafter referred to as NCD00]. The current paper is focused on the follow-up error attribution phase, in which the deficiencies in simulated circulation, in particular surface winds, are related to specific features of the GCM's heating error from diagnostic modeling. Such a double-pronged approach consisting of diagnostic analysis and modeling should facilitate GCM development.

ENSO variability in observations and CCM3 simulation is extracted from the rotated principal component analysis (RPCA) of combined variability of SST and 1000-mb (or surface) winds. In view of considerable similarity between the principal component and Niño-3.4 SST index variations (cf. Fig. 1), the extracted ENSO variability compares closely with the one isolated from regression with this SST index. ENSO covariant anomalies in other fields (e.g., wind at upper levels) are obtained from regression with the ENSO principal component, as in the earlier study.[3]

The salient features of most of the datasets used in this study (CCM3 simulation, ECMWF and NCEP reanalyses, and the Xie–Arkin precipitation) have been described in section 2 of NCD00. Discussion of residual diagnosis of 3D diabatic heating from atmospheric reanalyses, and aspects of the RPCA of combined variability are contained in section 3 of that paper.

This study begins with a brief description of the revised 1945–93 Comprehensive Ocean–Atmosphere Dataset (COADS; section 2), which is mainly used to corroborate the structure of ENSO surface wind anomalies in the shorter 1979–93 period. This period is of interest because both ECMWF and NCEP reanalyses are available in these years, and because comparisons of ENSO precipitation and vertically averaged heating anomalies show the ECMWF heating anomalies to be in greater structural accord with the independent Xie–Arkin precipitation anomalies (cf. Figs. 4 and 6 in NCD00). Diagnostic modeling of CCM3's ENSO circulation errors is thus undertaken with the ECMWF's circulation and diagnosed heating anomalies as validation targets. For this reason, the ECMWF reanalysis period, 1979–93, is particularly interesting.

ENSO wind stress variability in COADS observations and CCM3 simulation in the longer 1950-onward period is compared in section 3a, and the structure of ENSO surface (1000 mb) winds in ECMWF and NCEP reanalyses, and CCM3 simulation in the overlapping part of the records (1979–93) is compared in section 3b. The diagnostic multilevel global primitive equation model is

[3] ENSO variability was extracted from RPCA rather than simply from SST-index regressions because the non-ENSO modes were also of interest, although their discussion is beyond the scope of this paper.

Unauthenticated | Downloaded 02/21/24 05:03 PM UTC

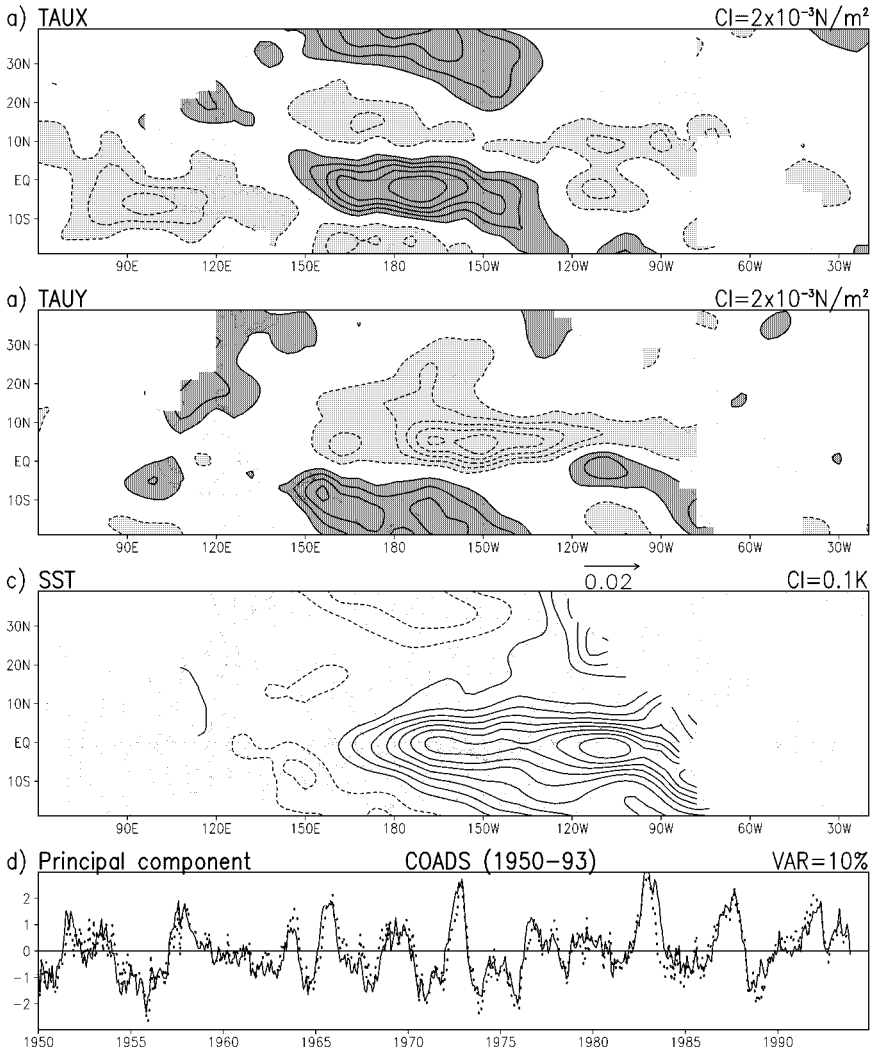

FIG. 1. Leading mode of combined variability from the rotated principal component analysis of COADS variables: (a) zonal wind stress τ_x, (b) meridional wind stress τ_y, (c) SST and wind stress vectors, and (d) the principal component (solid line). The Niño-3.4 SST index [dotted line in (d)] is plotted to confirm this mode's linkage with ENSO variability. Contour interval and shading threshold is 2×10^{-3} N m^{-2} in (a) and (b), and 0.1 K in (c). The scale for wind stress vectors is shown at the top of (c). Zero contours are omitted in all panels.

described in section 4. Diagnostic modeling of CCM3's ENSO surface-wind errors, which begins with the simulation of ENSO circulation in ECMWF reanalysis, is presented in section 5. Attribution of CCM3's surface-wind errors to specific features of its heating-distribution error is discussed in section 6. The contribution of longwave radiative heating in forcing ENSO surface winds in CCM3 is examined in section 7. Discussion and concluding remarks follow in section 8.

2. Revised COADS data

The revised COADS was developed by Da Silva et al. (1994) from the objective analysis of individual COADS observations on a $1° \times 1°$ grid during January 1945–December 1993. The dataset reduces the wind speed bias and artificial wind speed trends associated with an erroneous Beaufort equivalent scale. However, like other objectively analyzed COADS datasets, it suffers from sparseness of observations in the central and eastern equatorial Pacific where the occurrence of ''less than five wind observations per month per $1° \times 1°$ box'' is not uncommon, particularly in the early part of the record. The monthly SST and surface wind stresses[4] are

[4] Comparisons of surface wind stresses are sometimes preferable to those of surface winds especially when datasets can differ in the height at which surface winds are defined, and because it is the wind stresses that drive the oceanic circulation, particularly, in the Tropics.

Unauthenticated | Downloaded 02/21/24 05:03 PM UTC

linearly interpolated on to a 6° long × 2° lat grid in order to yield a manageable matrix in the combined variability analysis of these fields during the 1950–93 period.

3. ENSO surface-wind intercomparisons

a. COADS and CCM3 wind stress anomalies in longer-period analysis

ENSO variability in COADS observations (1950–93) and CCM3 simulation (1950–94) is compared in this section. In both cases, the patterns are obtained from RPCA of combined interannual variability of the Pacific basin SST and the zonal and meridional wind stresses (τ_x, τ_y) in the Pacific and adjoining ocean basins (60°E–20°W). Note that CCM3 simulation is produced using NCEP SSTs, which differ somewhat from COADS SSTs. The NCEP SSTs are produced from in situ observations and bias-corrected satellite SST data in the post-1981 years, and from empirical orthogonal function–based reconstruction in the earlier years [see section 8 in Kalnay et al. (1996)].

The leading variability mode in COADS is shown in Fig. 1. The SST-anomaly structure, and the similarity in the principal component and Niño-3.4 index evolutions indicate this to be the ENSO mode. The strongest westerly and equatorward wind stress anomalies occur eastward of the date line, just like the corresponding surface-wind anomalies (e.g., Deser and Wallace 1990; Nigam and Shen 1993). It is noteworthy, particularly in the context of subsequent intercomparisons, that observed wind stress variability in the eastern tropical Pacific is relatively weak, and that the off-equatorial easterly amplitudes are only one-fourth as large as the westerly amplitudes in the central equatorial Pacific.

The structure of ENSO variability in the CCM3 simulation is displayed in Fig. 2. Despite similar SST anomalies and principal component variations, CCM3's wind stresses differ significantly from the COADS ones: CCM3 stresses are about twice as strong in the central tropical Pacific, but in the eastern north-equatorial Pacific they are phenomenally strong—in contrast with COADS, where this region is relatively quiescent in wind stress activity. Easterly stresses in the off-equatorial central Pacific are also too strong relative to COADS, and as a fraction of the simulated westerly wind stress at the equator. The latter are too tightly confined, meridionally, in the CCM3 simulation. Given these deficiencies, the rather realistic simulation of the ENSO covariant westerly wind stresses in the North Pacific is somewhat surprising.

The *difference* between the simulated and observed ENSO wind stresses, shown in Fig. 3, highlight many of the features noted above in discussion of Figs. 1 and 2. The CCM3–COADS difference is large, often exceeding 50% of the COADS stresses! The CCM3 zonal wind stress departures are pronounced in the off-equatorial Tropics, with the easterly stresses being much too strong there. The meridional stress departures indicate stronger equatorward flow across the Pacific.[5]

Can these wind stress differences be attributed to the modest differences in the two ENSO SST anomalies (Figs. 1c and 2c)? Results from the shorter-period analysis, presented next, indicate otherwise.

b. ECMWF, NCEP, and CCM3 1000-mb wind anomalies during 1979–93

ENSO anomalies in the overlapping portion of the three datasets are compared here. ENSO variability was extracted by analyzing the 1000-mb wind and SST variability over the Pacific basin (125°E–75°W, 20°S–40°N). The surface-wind comparisons are shown in Fig. 4. As NCEP SSTs were used in each of the combined analyses, the SST differences are very small and thus not shown.

The CCM3–ECMWF differences in 1000-mb winds (Figs. 4a,b) highlight some of the same features that were noted above in the context of wind stress comparisons (Fig. 3), particularly, stronger equatorward flow and the accompanying stronger easterlies in the off-equatorial Tropics of CCM3. The CCM3–NCEP differences (Figs. 4c,d) are qualitatively similar, except that zonal wind departures are smaller in the equatorial date line sector, while the meridional ones are almost twice as large as before. The insignificant SST differences associated with these wind differences, particularly, in the CCM3–NCEP case where both models are driven by the same NCEP SSTs, suggests that the CCM3 surface-wind differences arise from variance in models' physics rather than SST boundary conditions.

The similarity in the structure of CCM3 surface-wind departures (from ECMWF and NCEP anomalies), and the correspondence between CCM3's surface-wind and wind stress departures (from COADS anomalies), are reassuring, but robustness of these departures (''signal'')

On the other hand, wind stress differences can arise solely from variations in the bulk-aerodynamic formulas, and so wind stress comparisons need to be supplemented by surface-wind comparisons, when possible, in order to understand fully the reasons for the differences.

[5] Although CCM3's wind stress departures are clearly large, how big are the uncertainties in observed wind stresses? A comparison of surface winds—the dominant input in wind stress computation—in the original and Da Silva et al.'s (1994) version of COADS provides one such estimate. The original COADS was obtained from Lamont Doherty Earth Observatory's Climate Data Library (http://ingrid.ldeo.columbia.edu/SOURCES/.COADS/), and ENSO surface winds were computed from both versions via Niño-3.4 regressions in 1958–92. The two anomalies differ rather insignificantly (≤0.2 m s^{-1}; not shown), with the zonal-wind differences being particularly small. The differences are smaller than the corresponding reanalysis differences (shown later in Figs. 4e–f).

Unauthenticated | Downloaded 02/21/24 05:03 PM UTC

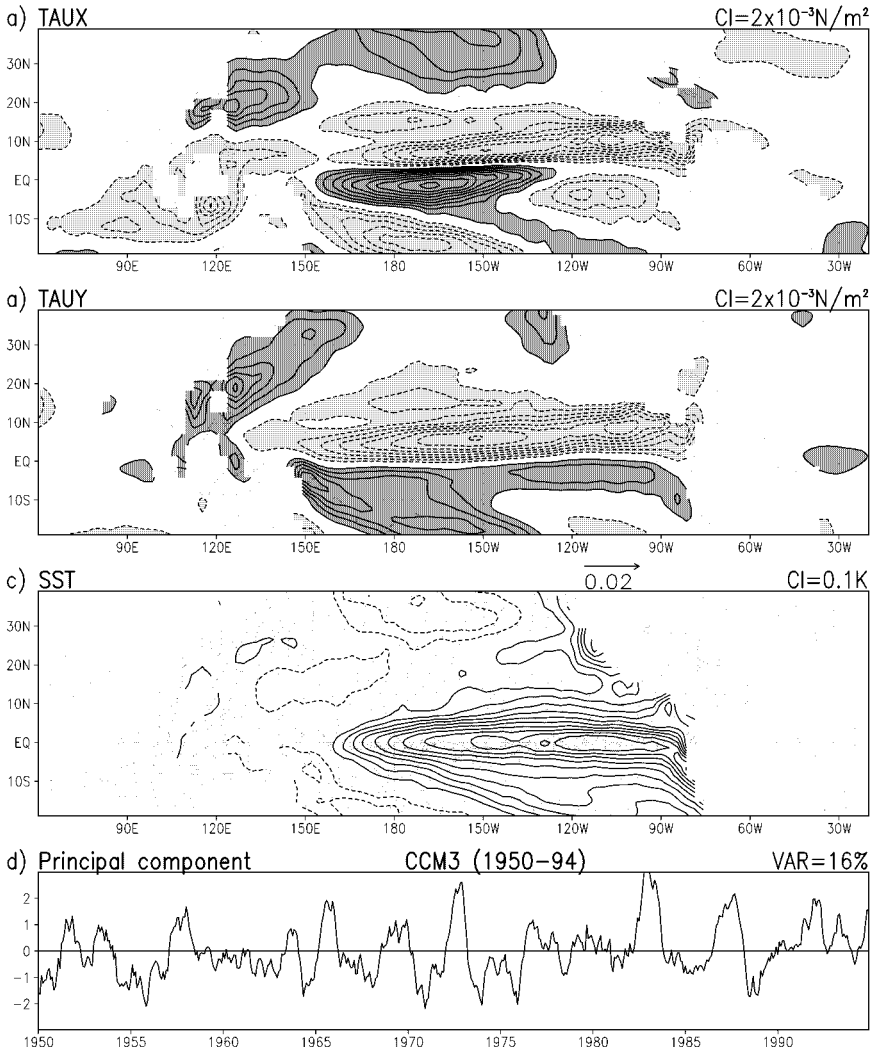

FIG. 2. As in Fig. 1, but from analysis of the CCM3 simulation (driven by 1950–94 NCEP SSTs).

should, perhaps, be gauged by comparing them with the difference of reanalysis anomalies themselves (''noise''; Figs. 4e,f). These differences, while not insignificant, are relatively modest; for example, they are smaller than half of the signal amplitude (Figs. 4a–d) in the central Pacific. In the eastern equatorial Pacific—the other region of notable disagreement—the ''noise'' amplitudes are even smaller, leading to a much larger signal-to-noise ratio. Even more compelling is the ''sign'' of the differences in Fig. 4, which shows the CCM3 anomalies to be outliers; for example, the ENSO covariant equatorward winds in the central Pacific are weakest in NCEP, and strongest in CCM3. Clearly, the CCM3 departures in ENSO surface winds can be characterized as errors.

The large amplitude ($\sim$1 m s^{-1}) and scale of ENSO surface-wind errors in CCM3 (Fig. 4), and the documentation of significant errors in its ENSO heating distribution (in NCD00) raise the possibility of dynamical linkage between the errors—a possibility investigated from diagnostic modeling analysis in the remainder of the paper. Although, the modeling analysis, by itself, will be unable to pinpoint the CCM3 physical parameterizations that need revision, it can implicate the heating error in a specific region, for example, lower troposphere or the off-equatorial subsidence zones, as the cause of surface-wind errors, thereby drawing attention to the heating parameterizations operative in those regions. The guidance provided by such diagnostic analysis and modeling however needs to be verified from controlled GCM simulation experiments, particularly, if the region of interest contains robust climate feedbacks.

4. Diagnostic primitive equation model

The global model solves the steady, σ coordinate ($\equiv p/p_s$, where p_s is surface pressure), primitive equa-

Unauthenticated | Downloaded 02/21/24 05:03 PM UTC

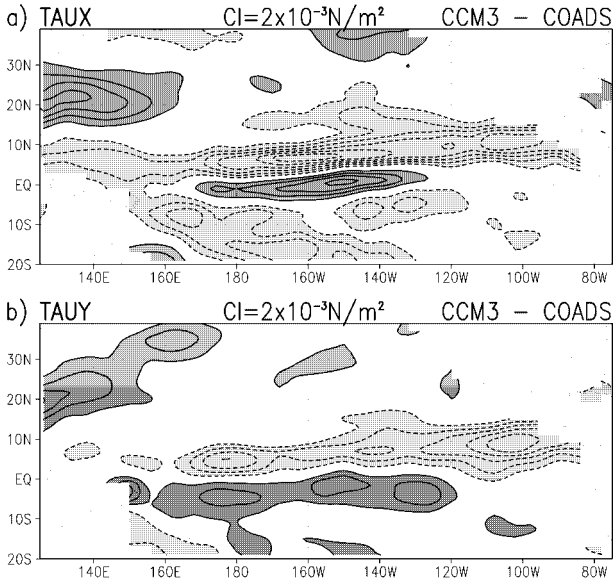

FIG. 3. ENSO wind stress *differences* between CCM3 simulation and COADS. Contour and shading as in Fig. 1.

tions. The equations are linearized about a zonally symmetric basic state, and thus model the *eddy* component (i.e., deviation from the zonal average) of circulation. The linearized model equations are given in the appendix of Held et al. (1989). In order realistically to represent the thermal and momentum diffusion processes in the planetary boundary layer, the simplified Rayleigh momentum-dissipation and Newtonian temperature-damping terms in these equations are replaced by linearized versions of the vertical momentum and thermal diffusion terms (Nigam 1997). The diffusion coefficients vary in the boundary layer, decreasing rapidly above 925 mb. The inclusion of diffusive mixing in the model leads to boundary conditions on zonal and meridional velocity, and temperature, which involve drag coefficients C_{DU}, C_{DV}, and C_{DT}.

In addition to vertical diffusive mixing in the planetary boundary layer, the thermodynamic and horizontal momentum equations include horizontal ∇^2 diffusive mixing, with a constant coefficient of 1×10^6 m^2 s^{-1}. Additional model details can be found in the appendix of Nigam (1994). All model parameters are specified exactly as in Nigam (1997), except for the drag coef-

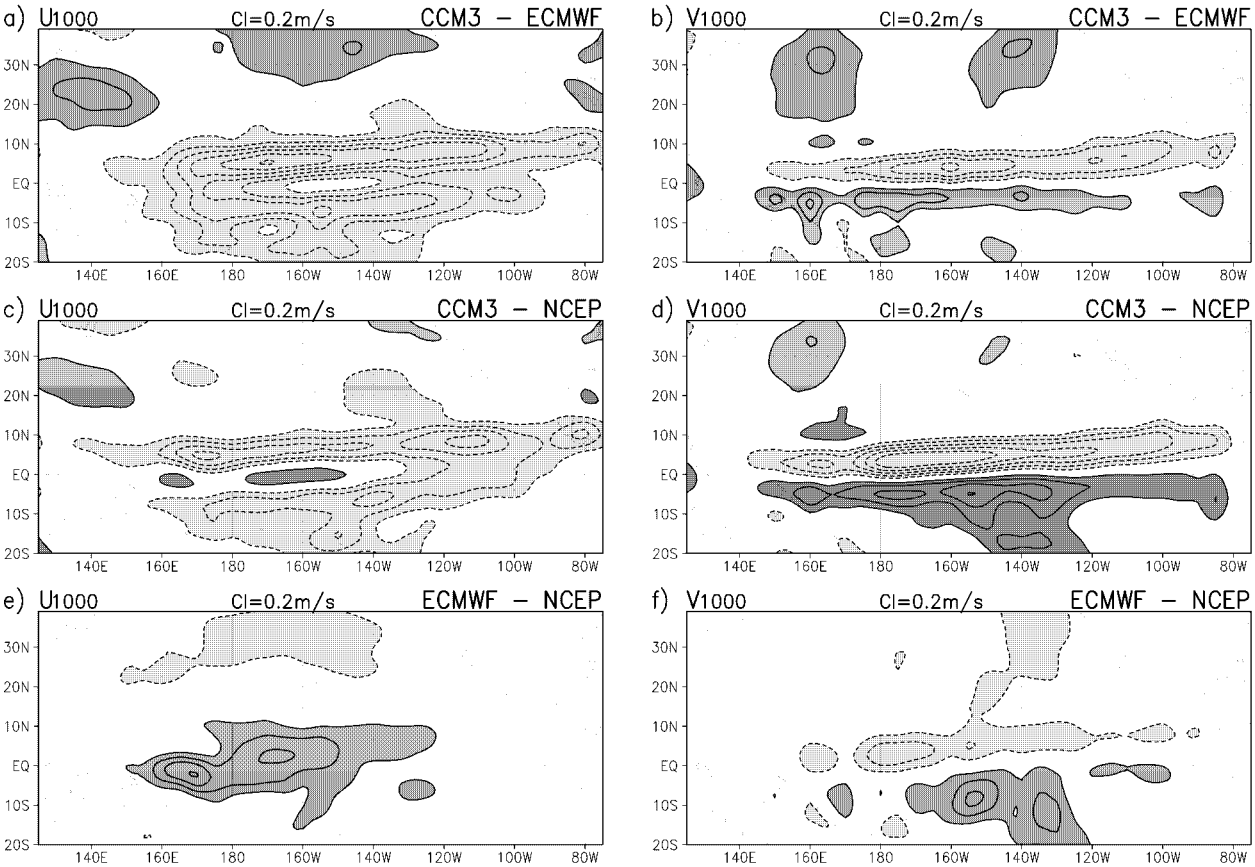

FIG. 4. ENSO surface-wind *differences* in the common period (1979–93) of CCM3 simulation, and ECMWF and NCEP reanalyses: (left) zonal-wind differences; (right) meridional differences. Contour interval and shading threshold is 0.2 m s^{-1}, and the zero contour is omitted as before.

Unauthenticated | Downloaded 02/21/24 05:03 PM UTC

ficients C_{DU} and C_{DV}, which are both set equal to 1.0×10^{-3} instead of 1.5×10^{-3}.

The diagnostic model is solved numerically, using the semispectral representation for the horizontal structure of variables: 73 grid points between the two poles ($\Delta\theta = 2.5°$), and zonal Fourier truncation at wavenumber 30 (equivalent to $\Delta\lambda = 6.0°$), where θ is latitude and λ is longitude. The vertical structure is discretized using 18 full-sigma levels[6] of which 14 are in the troposphere, including 5 below 850 mb. The semispectral model was preferred in view of the strong latitudinal variation of tropical features, such as the intertropical convergence zone (ITCZ).

The model equations are linearized about the zonally symmetric climatology (from the 1979–93 ECMWF reanalysis), which leads to uncoupling of zonal wavenumbers and speedy numerical solutions. The incomplete representation of linear anomaly dynamics (rectifiable by linearization about the zonally varying climatology) is potentially problematic for the modeling of upper-level flow in view of dynamical interactions between anomalous flow and the vorticity gradients of the climatological Pacific and Atlantic jets, particularly during northern winter. Although modeling of near-surface flow in the Tropics is immune from such concerns, the model's linearization about a zonal-mean climatology can be limiting even here, should zonal averaging efface planetary boundary layer (PBL) features, such as the capping inversion, which is generally present only over eastern sectors of the tropical oceans (under subsiding branches of the divergent Walker and Hadley circulations). Because this feature is unrepresented in the pressure-level reanalysis datasets on account of coarse sampling of the PBL ($\Delta p = 75$ mb), the model's basic state is chosen to be zonally symmetric in this study.

5. Diagnostic modeling of ENSO surface winds

Diagnostic modeling of the ENSO circulation anomalies in ECMWF reanalysis and CCM3 simulation is described here. Our focus is on modeling the CCM3 departures from ECMWF anomalies, that is, the error in CCM3's ENSO response, particularly, at the surface (1000 mb). If notable features of the circulation error can be simulated, then their origin can be ascertained, at least, in a diagnostic (a posteriori) sense. For a meaningful analysis, however, the model should be required to simulate the individual ENSO responses as well. The diagnostic model is reasonably successful in all these cases, and as evidence we show the simulation of the ECMWF ENSO response and the CCM3–ECMWF ENSO circulation. We chose to display the simulation of ECMWF's rather than CCM3's ENSO response in order to highlight the quality (or dynamical consistency) of the residually diagnosed 3D diabatic heating, which dominates tropical forcing during ENSO.

a. Simulation of ECMWF's ENSO circulation

The diagnostic simulation of the ECMWF ENSO circulation is shown in Fig. 5. The simulation (Figs. 5a–c) is forced by the 3D ENSO diabatic heating anomalies in the 30°S–30°N belt, and by the ''model sensible heating'' resulting from vertical thermal diffusion of ENSO SST anomalies (specified at the model's lower boundary). The 3D heating was residually diagnosed from ECMWF reanalyses, and the ENSO covariant anomalies were displayed in NCD00 (see their Figs. 2a, 4a, 8a, and 10).

The diagnostic model solves for the eddy, or zonally asymmetric, flow component, as noted earlier in section 4. Simulation targets from ECMWF reanalysis are thus shown in Figs. 5d–f, after removal of their zonal-mean part. The simulated ENSO winds and divergence at 1000 mb compare closely with their targets, indicating the rather limited contribution of the excluded forcing (from submonthly thermal and momentum transients, and extratropical diabatic heating anomalies). Note that simulated flow is slightly weaker, particularly, meridional wind. The modeled divergence is thus also weaker, but the equatorward shift of ITCZ and the South Pacific convergence zone in ECMWF anomalies (Fig. 5f) is captured in the linear simulation (Fig. 5c). The circulation anomalies over the Indian Ocean are also modeled with reasonable fidelity.

The contribution of model sensible heating in the simulated ENSO anomalies is nontrivial in case of meridional wind and divergence, as apparent from Fig. 6; note however that contour intervals here are half of those in Fig. 5. In the central and eastern equatorial Pacific, up to one-third of the V_{1000} and DIV_{1000} amplitudes can be ascribed to this contribution. It is, however, likely that this heating component's contribution would be even more significant in a model whose basic state included the PBL-capping inversion present in this sector's climatology. Indeed, preliminary calculations conducted with a zonal-mean basic state containing an idealized PBL inversion (to be reported elsewhere) indicate this to be the case.

Can the sensible heating's impact be overrepresented in the diagnostic simulation (Figs. 5a–c) since this heating component is implicitly included in the residually diagnosed diabatic heating anomalies? The chances of overrepresentation, or ''double counting,'' are slim for various reasons. Sensible heating would be fully represented in the residually diagnosed heating anomalies provided the planetary boundary layer was adequately sampled by the 17 pressure-level ECMWF reanalyses; in this dataset, the first upper-air level is at 925 mb. Model sensible heating, on the other hand, should be largely confined to the 1000–925-mb layer, because the

[6] The 18 full-sigma levels are: 0.025, 0.075, 0.125, 0.175, 0.225, 0.275, 0.325, 0.375, 0.425, 0.498, 0.594, 0.6885, 0.7775, 0.8565, 0.9205, 0.9605, 0.9815, 0.995.

Unauthenticated | Downloaded 02/21/24 05:03 PM UTC

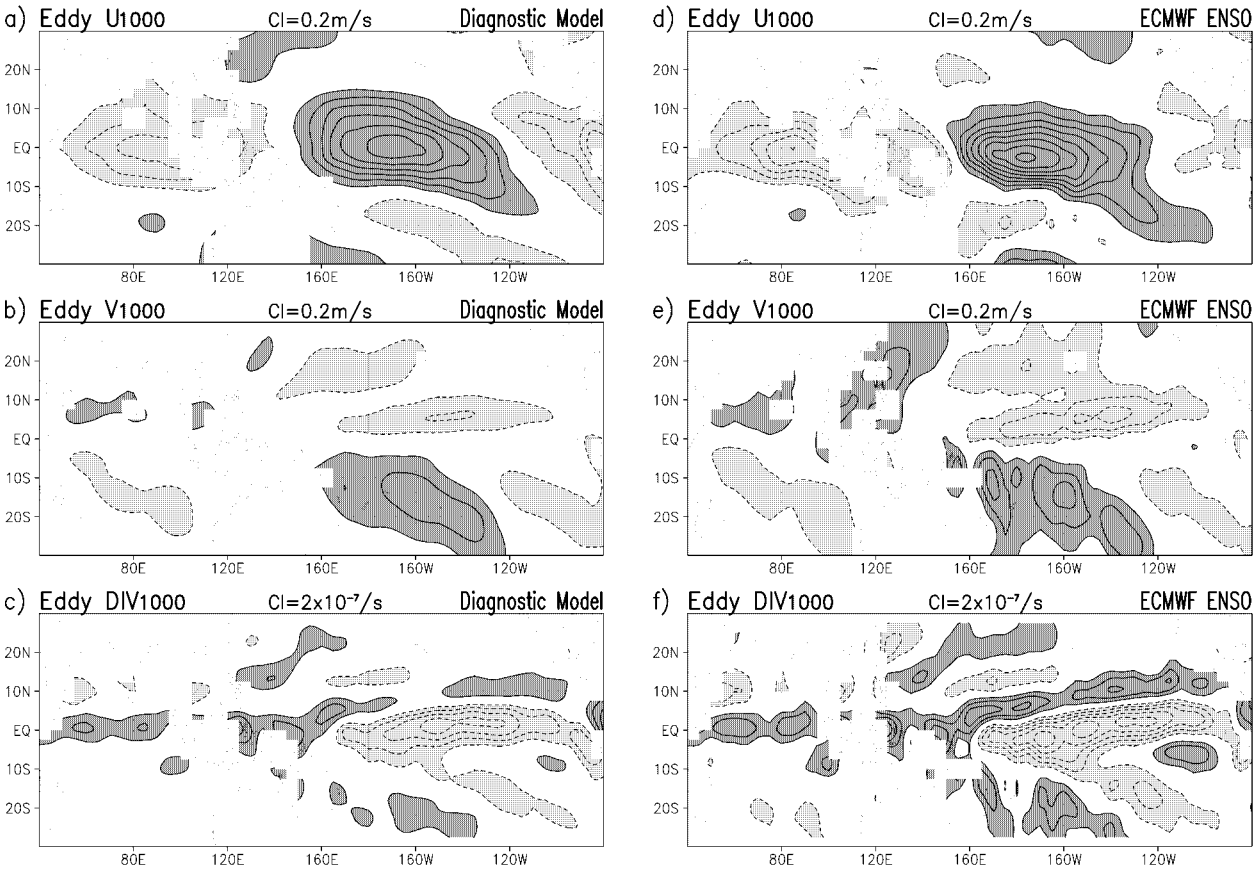

FIG. 5. ENSO surface winds and divergence over the Pacific and Indian sectors: (left) diagnostic model's response forced by ENSO heating ($|\theta| \leq 30°$; diagnosed from ECMWF reanalysis) and model sensible heating (cf. section 5a); (right) the corresponding ENSO covariant fields in ECMWF reanalysis. Contour interval and shading threshold is 0.2 m s^{-1} for winds and 2.0×10^{-7} s^{-1} for divergence, and the zero contour is omitted. Note that model predicts only the zonally asymmetric component of the flow, and thus only this part is compared.

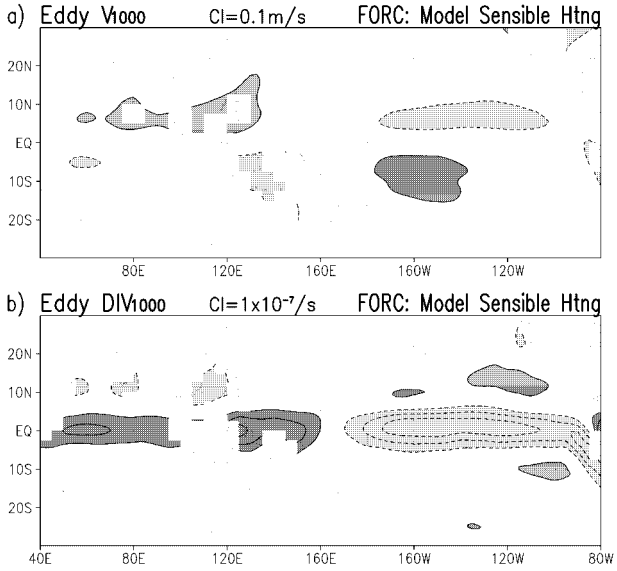

FIG. 6. Meridional wind and divergence forced by model sensible heating alone. The heating is generated from vertical thermal diffusion of ENSO SST in the diagnostic model's boundary layer. Note that contour intervals and shading thresholds are *half* of those in Fig. 5.

vertical diffusion coefficient diminishes rapidly above this level (cf. section 4).[7] To confirm that the impact of sensible heating was not overrepresented, another simulation was obtained, this time with the diagnosed heating anomalies set equal to zero in the planetary boundary layer ($\sigma \geq 0.888$, or $p \gtrsim 880$ mb). The simulation turned out to be very similar to the previous one (Figs. 5a–c)—within 5%–10% of it—confirming that the sensible heating impact was not significantly overrepresented in Figs. 5a–c.

In any case, double counting of the sensible heating's impact is a nonissue in the diagnostic simulation of circulation *error*, because the latter is obtained from the difference of two linear simulations, each using the same SST boundary condition. The model sensible heating contribution is thus zero in this simulation.

[7] Note that model sensible heating cannot be entirely eliminated because some thermal (and mechanical) dissipation is required to keep the model's matrix nonsingular, and thus invertible. Apart from these ''numerical'' reasons, the model must provide a pathway for thermal dissipation, for physical reasons.

Unauthenticated | Downloaded 02/21/24 05:03 PM UTC

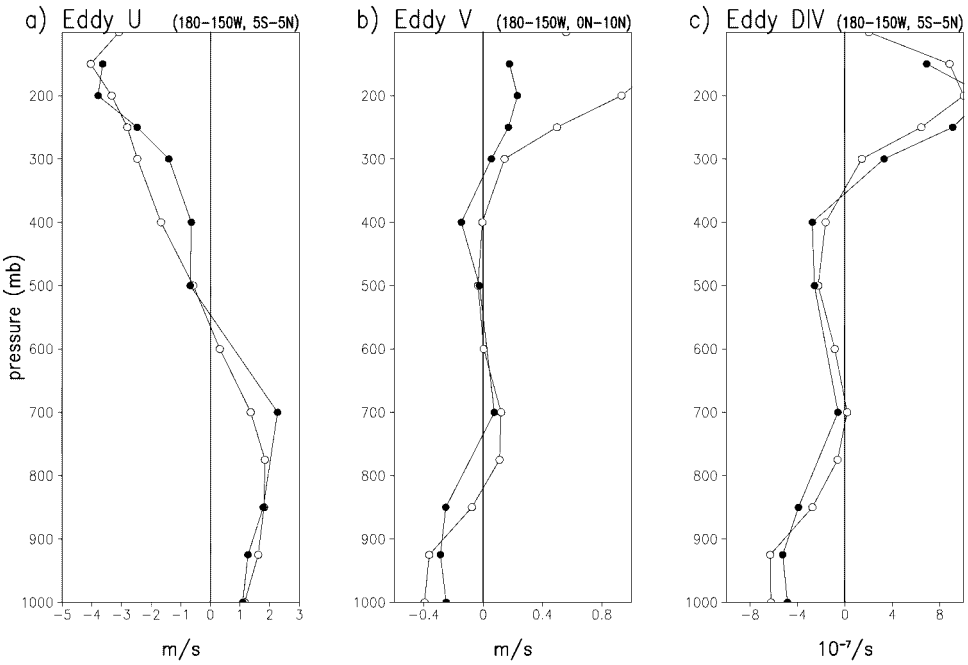

FIG. 7. Vertical structure of ENSO winds and divergence in the indicated central Pacific sectors: diagnostic simulation is shown by "●," while the corresponding ECMWF reanalysis profiles are shown by "○."

Although quite satisfactory, the quality of surface-wind simulation alone is not enough to establish the credibility of the diagnostic model. The upper-air simulation is therefore examined in Fig. 7. Vertical profiles of wind and divergence are displayed in sectors chosen on the basis of the 1000-mb anomaly structure (Fig. 5): U and DIV in the central equatorial Pacific (5°S–5°N, 180°–150°W), and V in the north-equatorial central Pacific (EQ–10°N, 180°–150°W). The simulation ("●" markings) compares quite favorably with the ECMWF anomalies ("○" markings) except in the upper troposphere where excluded forcing by transients and extratropical heating, and the model's linearization about the zonally symmetric basic state, begin to limit the simulation quality. The simulation in the lower troposphere is, however, quite reasonable, although the planetary boundary layer is slightly deeper, as is apparent particularly in the V profile. It is worth noting that while both U and V exhibit an internal-mode-type vertical structure, there are significant differences: the inflow and outflow regions in the V profile are much shallower.

The modeled divergence (Fig. 7c) compares favorably with the ECMWF profile, even in the upper troposphere. In view of the dominant thermodynamic balance in the Tropics between diabatic heating and adiabatic cooling ($-N^2\omega \sim Q/c_p$), horizontal divergence ($=-\partial\omega/\partial p$) is related to the vertical heating gradient: $\nabla_h \cdot \mathbf{V} \approx \partial[Q/(c_p N^2)]/\partial p$. Such a relationship can be visually ascertained by comparing the ECMWF DIV and Q profiles (the latter is shown in Fig. 10 of NCD00). The similar structure of the ECWMF V_{0-10N} and DIV_{5S-5N} profiles (Fig. 7), moreover, indicates that equatorial divergence is dynamically generated, largely, from the $\partial V/\partial y$ term.

The considerable correspondence between the simulated and observed circulation anomalies attests both to the dynamical consistency of residually diagnosed diabatic heating (from ECMWF reanalysis) and the diagnostic model's potential in analyzing the forcing of ENSO surface winds.

b. *Simulation of the CCM3–ECMWF ENSO circulation*

The diagnostic simulation of the departure of CCM3's ENSO circulation from its ECMWF counterpart is shown in Figs. 8a–c; the CCM3 circulation errors are forced by ENSO heating differences in the 30°S–30°N belt. Comparisons with the target fields (difference in ENSO regressions with CCM3 simulation and ECMWF reanalysis data; shown in Figs. 8d–f) indicate that diagnostic model has simulated the overall structure of CCM3 errors, but not their amplitude; note that target fields are contoured with twice the interval, and are somewhat more meridionally confined. The notable features of CCM3's surface-wind errors, namely, stronger easterlies in the off-equatorial Pacific and westerlies over the Indian Ocean, and enhanced equatorward flow in the central Pacific and poleward flow over the "Maritime Continent" have, however, all been modeled. Stronger convergence over the equatorial Pacific, and divergence over the equatorial Indian Ocean, Maritime Continent, and the off-equatorial Pacific have also been

Unauthenticated | Downloaded 02/21/24 05:03 PM UTC

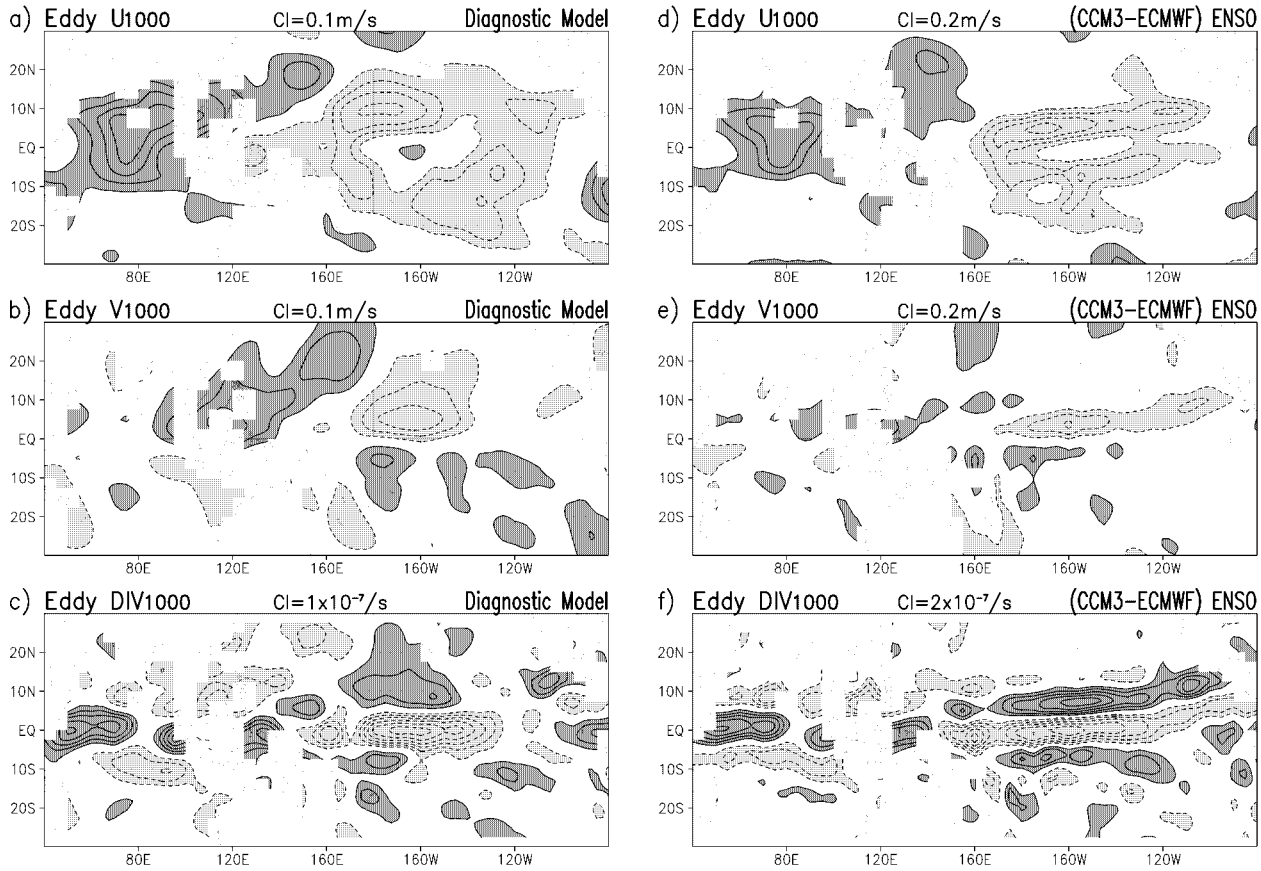

FIG. 8. ENSO circulation *difference* between CCM3 and ECMWF reanalysis: (left) diagnostic simulation forced by the CCM3–ECMWF heating in the Tropics; (right) the difference between the CCM3 and ECMWF ENSO loading vectors (or EOFs). Contour interval and shading threshold is 0.1 m s^{-1} for winds and 1.0×10^{-7} s^{-1} for divergence in the diagnostic solutions, and *twice* as large in the target fields. Zero contour is omitted as before.

captured in the diagnostic simulation, but with diminished amplitudes (cf. Figs. 8c and 8f).

6. Attribution of CCM3's surface-wind error

The attribution of circulation error features to aspects of the forcing error, from linear diagnostic modeling, is a viable strategy in the Tropics because the horizontal structure of forcing (principally heating) is strongly influenced by the underlying SST structure. If the forcing structure, however, evolved in response to the anomalous flow itself—a strong possibility in the extratropics because of stormtrack modulation, for example—the insights obtained from diagnostic modeling would need to be reevaluated from controlled GCM simulation experiments.

A prerequisite for this analysis strategy is a credible simulation of CCM3's circulation error, and the diagnostic simulation is quite satisfactory in this regard, as documented in section 5. It is worth emphasizing that it is the linearized dynamics of the diagnostic model that allows decomposition of forcing (heating error in this case) into parts that can be potentially attributed as source of the various circulation error features, while retaining dynamical consistency between the *total* forcing and circulation error fields.

The decomposition of CCM3's heating error in subsequent linear modeling analysis is guided by the structure of its salient features, which were noted in the introduction. CCM3's ENSO heating distribution was extensively compared with the diagnosed ones from ECMWF and NCEP reanalysis in NCD00. The robust features of CCM3's ENSO heating *error* are the following:

- Strong diabatic cooling in the off-equatorial Tropics from a more ''Hadley-like,'' or meridional, ENSO heating redistribution in CCM3, with the Xie–Arkin precipitation anomalies confirming this assessment (cf. Figs. 5 and 6 in NCD00).
- Strong heating in equatorial (and cooling in off-equatorial) latitudes, particularly in the lower troposphere (600–850 mb), from a ''bottom-heavy'' CCM3 heating profile (cf. Figs. 9 and 10 in NCD00); the 700-mb *error* is larger than the diagnosed heating anomalies themselves!

Unauthenticated | Downloaded 02/21/24 05:03 PM UTC

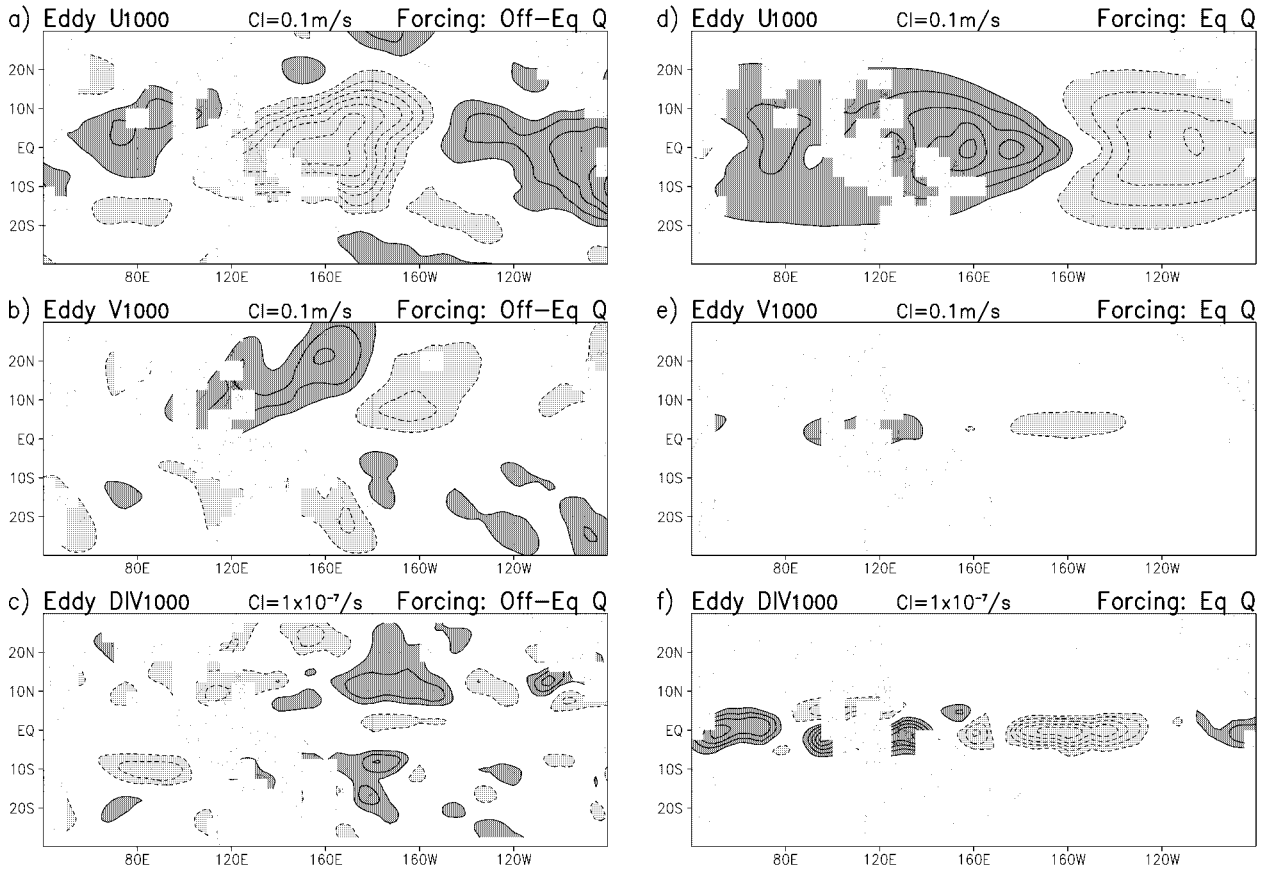

FIG. 9. (left) Diagnostic model's response forced by ENSO heating *differences* (CCM3–ECMWF) in the off-equatorial latitudes ($5° < |\theta| < 30°$). (right) The model response forced by equatorial ($|\theta| \leq 5°$) differences. Contour interval and shading threshold is 0.1 m s^{-1} for winds and 1.0×10^{-7} s^{-1} for divergence in all panels, and the zero contour is omitted as before.

- Strong heating over the eastern equatorial Indian Ocean, Borneo, the Philippines, and the South China, Sulu, and Celebes Seas, from weak ENSO diabatic cooling over this region in CCM3 (cf. Figs. 2–6 in NCD00).

The surface-wind impact of each of these heating error features is examined here. The impact of stronger meridional redistribution of heating is evaluated first, by computing responses of the off-equatorial ($5° < |\theta| < 30°$) and equatorial ($|\theta| \leq 5°$) parts of the heating error; the responses are shown in the left and right panels of Fig. 9, respectively. Comparison with the response of total heating error (shown earlier in Figs. 8a–c) indicates that almost all of the meridional wind error (Fig. 8b) results from the heating error in off-equatorial latitudes. Excessive cooling in this sector also produces much of the easterly wind and surface-divergence errors in the off-equatorial Pacific.

The generated surface-wind response (Figs. 9a–c) can be physically understood as follows: Excessive diabatic cooling in the off-equatorial Tropics is balanced by subsidence-induced adiabatic warming. Subsidence leads to surface divergence and equatorward flow, which in turn produces easterly winds from Coriolis turning, and convergence at the equator.

Heating error in the equatorial belt, on the other hand, accounts for aspects of easterly error in the central and eastern tropical Pacific, and for over half of the westerly error in the tropical Indian ocean (Fig. 9d). The remaining westerly error in this region is generated by the off-equatorial portion of the heating error (Fig. 9a). Not surprisingly, most of the equatorial divergence error (Fig. 8c) is forced by the local heating error (Fig. 9f).

The surface-wind impact of the ''bottom-heavy'' feature of CCM3's equatorial heating profile is examined next, by calculating the diagnostic model's response to two equatorial ($|\theta| \leq 5°$) heating distributions. The heating fields were generated from the same horizontal structure—the mass-weighted vertical average (1000–100 mb) of CCM3's ENSO heating anomalies—but using different profiles (CCM3 and ECMWF; cf. Fig. 10 in NCD00) in the vertical. The difference in model solutions forced by these heating distributions is shown in Figs. 10a–c. Evidently, more than half of the *zonal*-wind response forced by CCM3's equatorial heating error (Fig. 9d) can be attributed to the differences in *vertical*

Unauthenticated | Downloaded 02/21/24 05:03 PM UTC

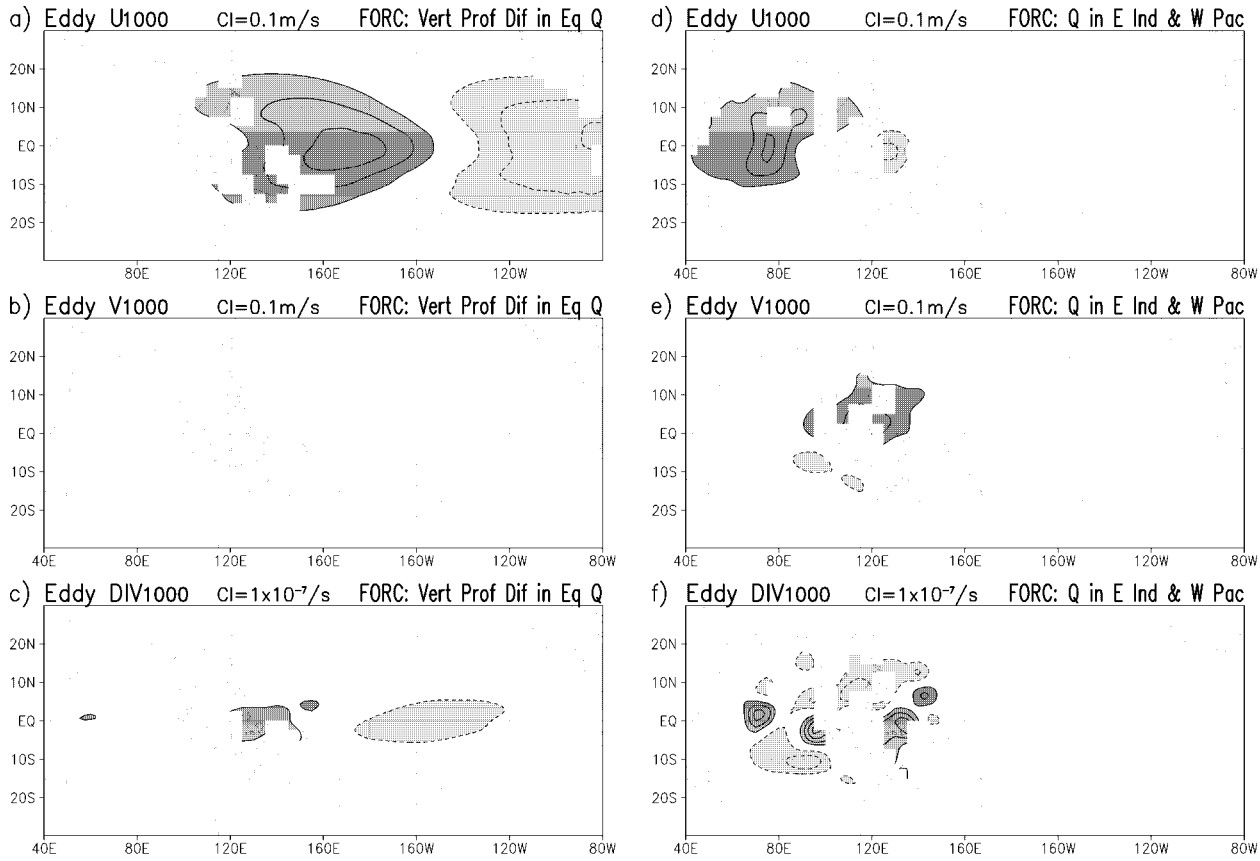

FIG. 10. (left) Diagnostic model's response forced by the heating *difference* resulting from differences in CCM3 and ECMWF vertical heating profiles (see section 6 for additional details). (right) The model response forced by ENSO heating *differences* in the eastern Indian and western Pacific sectors ($65°E < \lambda < 150°E$ and $20°S < \theta < 20°N$). Contour interval and shading as in Fig. 9.

structure of CCM3 and ECMWF heating fields. An accurate portrayal of the vertical structure of equatorial heating would thus appear necessary for modeling ocean–atmosphere interactions, given the important role of *zonal* wind stress in driving oceanic circulation in the Tropics.

The surface-wind response of the heating error resulting from weak diabatic cooling over the eastern Indian Ocean, Maritime Continent, and the western Pacific is shown in Figs. 10d–f. We focus on this region by setting the heating error to zero outside the $65°E < \lambda < 150°E$ and $20°S < \theta < 20°N$ sectors. In this diagnostic assessment, the regional heating error generates local surface-wind and divergence errors, which contribute substantially to the total circulation errors in this region (cf. Figs. 8a–c).

In summary, diagnostic modeling has implicated the heating error features noted above in the generation of key surface-wind errors in CCM3's simulation of ENSO variabilty. In one sense, this implication is not all that profound, given the strong linkage of 3D heating and surface winds in the Tropics. However, demonstration of dynamical linkage between *specific* features of the CCM3's ENSO heating distribution and characteristic features of the accompanying surface-wind errors is nontrivial and potentially insightful in developing strategies for GCM improvement.

7. Longwave radiative forcing of ENSO surface winds in CCM3

The role of longwave heating in forcing surface winds in the CCM3 Tropics is examined here. Longwave heating is the second-largest ENSO covariant heating component among five that are archived in the CCM3 simulation (see section 2c in NCD00). Moreover, its distribution during ENSO peaks in the lower troposphere (near 800 mb; see Fig. 12b in NCD00). It is this proximity to the surface that primarily motivates the present analysis.

The significance of longwave heating in forcing surface winds has been recognized before (e.g., Nigam 1997), but in context of seasonal-cycle variability in the eastern tropical Pacific. In that case, longwave anomalies arose from the radiational cooling-to-space from stratus cloud tops (~850 mb) in the large-scale subsidence zones. In case of ENSO variability, however, the anomalies result from the trapping of longwave radia-

Unauthenticated | Downloaded 02/21/24 05:03 PM UTC

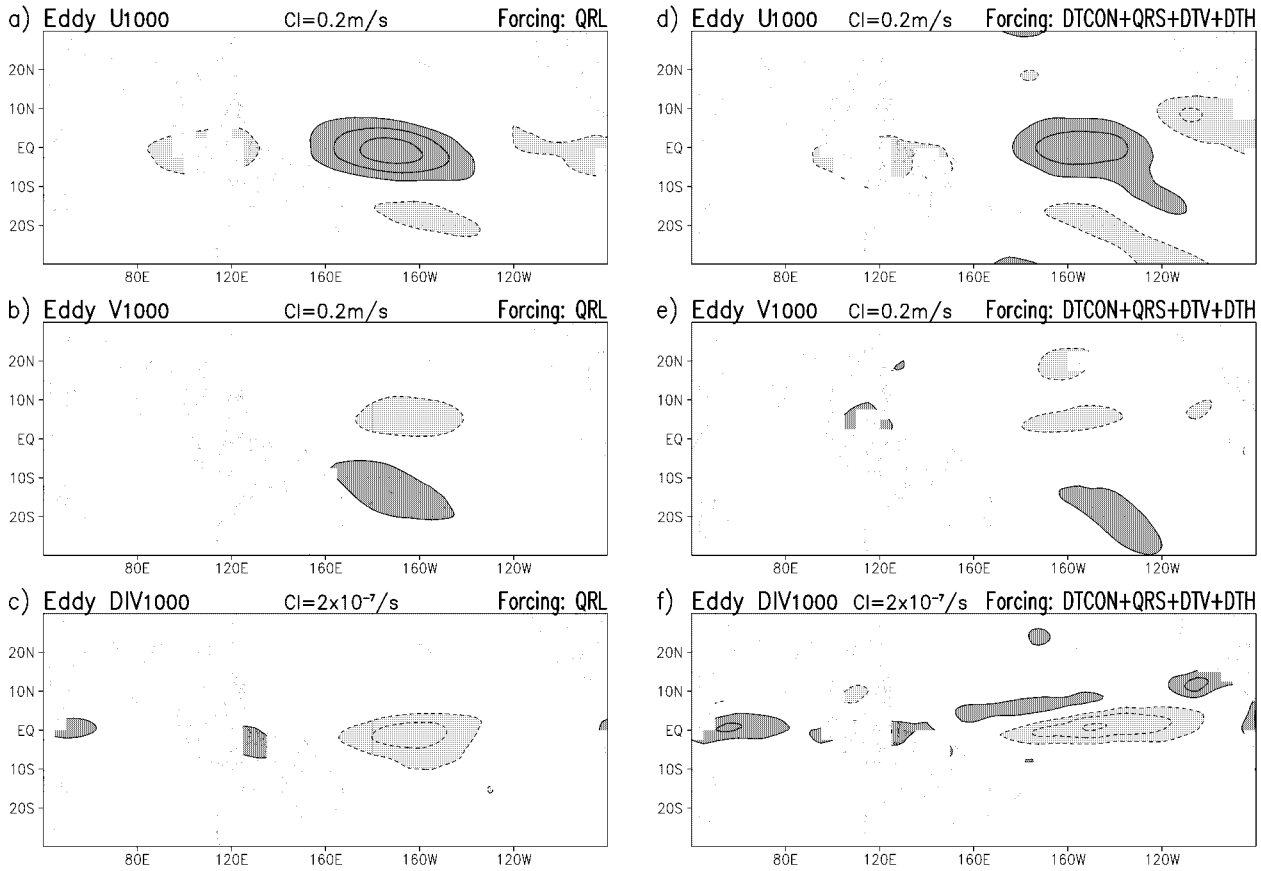

FIG. 11. (left) Diagnostic model's response forced by the ENSO covariant longwave radiative heating in CCM3. (right) The model solution forced by all other CCM3 heating components. Contour interval and shading threshold is 0.2 m s^{-1} for winds and 2.0 $\times$ 10^{-7} s^{-1} for divergence in all panels, and the zero contour is omitted as before.

tion beneath cumulus/cumulonimbus clouds in the deep-convective zones; longwave cooling near cloud tops occurs here as well, but the cloud tops are much higher in this case, in the upper troposphere.

The diagnostic model's response to ENSO covariant longwave heating (QRL) and to the sum of the remaining heating components is shown in Fig. 11.[8] The impact of longwave heating on central Pacific surface winds and divergence (Figs. 11a–c) is evidently stronger than the response of all other heating components combined (Figs. 11d–f) in CCM3's simulation of ENSO variability! That the patterns displayed in the left and right panels have considerable similarity is also interesting. Surely, the correspondence in horizontal structure of the longwave (QRL) and condensation heating (DTCOND) anomalies—key model forcings in the Fig. 11 simulations—must be consequential in this regard. The heating correspondence is displayed in Figs. 12a,b of NCD00.

The longwave's influence, in fact, dominates boundary layer flow until ~800 mb, especially in zonal wind (not shown). Whether ENSO longwave heating substantially impacts the tropical near-surface winds in nature, however, remains to be ascertained. Diagnostic modeling with heating components from the reanalysis model's 6-h (or shorter) forecasts can provide preliminary answers to this question.

8. Discussion and concluding remarks

Diagnosing the reasons for deficient structure of interannual variability in a coupled GCM integration is a challenging task for climate diagnosticians. In view of myriad feedbacks and interactions between modeled climate processes, there is not a unique strategy for unraveling the source of errors that eventually lead to unphysical structure of climate variability. Conceptually, the diagnosis of the component GCMs (e.g., atmospheric GCM) is equally difficult because they too model the interactions between physical processes, albeit fewer of them. In the absence of a road map, where does one begin?

In this study, the reasons for deficient structure of

[8] The remaining four CCM3 heating components are solar heating (QRS), latent heating from all condensation processes (DTCOND), and heating from horizontal and vertical diffusion of temperature (DTH and DTV, respectively; cf. section 2c in NCD00).

Unauthenticated | Downloaded 02/21/24 05:03 PM UTC

interannual variability in an extended CSM integration are investigated by examining if one of the *necessary* conditions for obtaining realistic variability is fulfilled. The condition of interest in context of ENSO variability is the requirement of a high quality simulation of surface winds by the atmospheric component of CSM (CCM3) when forced by observed SSTs at the lower boundary, that is, in an uncoupled mode. (If this condition was met, one would be obligated to examine the fulfillment of other pertinent prerequisites in order to uncover the reasons for CSM deficiencies.)

The undertaken analysis shows that the necessary condition of high quality simulation of ENSO surface-wind variability is *not* met by the CCM3 model. The case is made using multiple validation targets, which incidentally allows estimation of uncertainty in the target fields. CCM3's ENSO wind stress was compared with COADS's in the longer period (1950–93) analysis, while ENSO surface (1000 mb) winds in the CCM3 simulation, and ECMWF and NCEP reanalysis were intercompared in the shorter but overlapping part of the records (1979–93).

CCM3's surface-wind departures (from reanalysis anomalies) were found to be structurally similar, both among themselves and to the CCM3 wind stress departures. Departure amplitudes (signal) were moreover larger than the difference of reanalysis anomalies themselves (noise) over most of the Pacific. CCM3's surface-wind departures were thus characterized as *errors*.

In a companion paper, the authors make a compelling case for the presence of robust errors in CCM3's ENSO heating distribution, based on comparisons with the residually diagnosed heating anomalies from ECMWF and NCEP reanalyses. The key errors among them are excessive diabatic cooling in the off-equatorial Tropics from a more Hadley-like, or meridional, ENSO heating redistribution, and strong heating in the equatorial (and cooling in off-equatorial) latitudes, particularly in the lower troposphere (600–850 mb), from a bottom-heavy CCM3 heating profile.

The occurrence of robust errors in both surface-wind and heating distributions in CCM3's simulation of ENSO variability raises the issue of linkage, which is investigated using a steady, linear, global, primitive equation model (18 vertical σ levels, 30 zonal waves, and $\Delta\theta = 2.5°$). The model is quite successful in simulating the ENSO circulation anomalies in ECMWF reanalysis and CCM3 simulation, and thus, in simulating CCM3's surface-wind *errors.*

Diagnostic modeling indicates strong linkage between the prominent error features. Stronger equatorward flow in the Pacific results largely from excessive diabatic cooling in the off-equatorial Tropics, a key heating error linked to a more meridional redistribution of ENSO heating in CCM3. The heating error also produces much of the easterly wind and surface-divergence errors in the off-equatorial Pacific in this diagnostic assessment. The bottom-heavy structure of CCM3's equatorial heating anomalies, on the other hand, is implicated in the generation of zonal-wind errors in the central and eastern tropical Pacific. In the diagnostic simulation of CCM3's ENSO variability, the longwave heating anomalies, with peak values near 850 mb, contribute as much to surface zonal winds as all other heating components together—a novel finding, needing corroboration from modeling analyses that include, among others, representation of key PBL features (e.g., capping inversion) in the model's climatological basic state.

Demonstration of dynamical linkage between heating and circulation errors is, in a sense, not all that profound, given the strong relationship between 3D heating and surface winds in the Tropics. However, modeling evidence linking *specific* features of the CCM3's ENSO heating distribution with characteristics of the accompanying surface-wind errors is potentially insightful in developing strategies for GCM's improvement.

The dynamical diagnosis strategy—consisting of diagnostic analysis of circulation and forcing, particularly, comparisons with observed/diagnosed counterparts, and follow-up dynamical modeling to understand the reasons for GCM's simulation deficiencies—will, by itself, be unable to pinpoint the CCM3 physical parameterizations that need revision. It can, however, implicate heating error in a specific region as the cause of surface-wind errors, thereby drawing attention to the heating parameterizations operative in that region. The guidance provided by such diagnostic analysis and modeling, however, needs to be verified from controlled GCM simulation experiments, particularly if the region of interest contains robust climate feedbacks.

It would be premature to attribute the CSM's unrealistic structure of interannual variability to CCM3's ENSO surface-wind errors without ascertaining the oceanic impact of the latter. The NCAR Climate System ocean model could be integrated in the climate simulation mode (i.e., uncoupled), once using the observed record of surface wind stresses and fluxes, and again with the identified ENSO surface-wind errors additionally included (prior to wind stress determination).

Acknowledgments. This research effort was supported by NSF Grants ATM 9422507 and 9906460 to S. Nigam. Chul Chung's doctoral research was supported, in part, by a NASA Graduate Student Fellowship in Global Change Research (Award NGT 30276). S. Nigam would like to thank Dave Randall and Maurice Blackmon for their encouragement and support of CCM3 diagnosis.

The authors would like to thank Ilana Stern of the data support group and the CCM3 consulting group at NCAR for help in accessing the ECMWF and CCM3 datasets. They would also like to thank Eric DeWeaver and Muthuvel Chelliah for facilitating access to some of the NCEP reanalysis datasets.

These research findings were presented at the Third Annual NCAR Climate System Model Workshop held in Breckenridge, Colorado (22–24 June 1998).

Unauthenticated | Downloaded 02/21/24 05:03 PM UTC

REFERENCES

Boville, B. A., and P. R. Gent, 1998: The NCAR Climate System Model, version one. *J. Climate,* **11,** 1115–1130.

Chung, C., and S. Nigam, 1999: Asian summer monsoon–ENSO feedback on the Cane–Zebiak model ENSO. *J. Climate,* **12,** 2787–2807.

Da Silva, A. M., C. C. Young, and S. Levitus, 1994: *Algorithms and Procedures.* Vol. 1, *Atlas of Surface Marine Data 1994,* NOAA Atlas NESDIS 6, NOAA, 83 pp.

Deser, C., and J. M. Wallace, 1990: Large-scale atmospheric circulation features of warm and cold episodes in the tropical Pacific. *J. Climate,* **3,** 1254–1281.

Held, I. M., S. W. Lyons, and S. Nigam, 1989: Transients and the extratropical response to El Niño. *J. Atmos. Sci.,* **46,** 163–174.

Hurrell, J. W., J. J. Hack, B. A. Boville, D. L. Williamson, and J. T. Kiehl, 1998: The dynamical simulation of the NCAR Community Climate Model version 3 (CCM3). *J. Climate,* **11,** 1207–1236.

Kalnay, E., and Coauthors, 1996: The NCEP/NCAR 40-Year Reanalysis Project. *Bull. Amer. Meteor. Soc.,* **77,** 437–471.

Meehl, G. A., and J. M. Arblaster, 1998: The Asian–Australian monsoon and El Niño–Southern Oscillation and the NCAR Climate System Model. *J. Climate,* **11,** 1356–1385.

Nigam, S., 1994: On the dynamical basis for the Asian summer monsoon rainfall–El Niño relationship. *J. Climate,* **7,** 1750–1771.

——, 1997: The annual warm to cold phase transition in the eastern equatorial Pacific: Diagnosis of the role of stratus cloud-top cooling. *J. Climate,* **10,** 2447–2467.

——, and H.-S. Shen, 1993: Structure of oceanic and atmospheric low-frequency variability over the tropical Pacific and Indian Oceans. Part I: COADS observations. *J. Climate,* **6,** 657–676.

——, C. Chung, and E. DeWeaver, 2000: ENSO diabatic heating in ECMWF and NCEP reanalyses, and NCAR CCM3 simulation. *J. Climate,* **13,** 3152–3171.

Xie, P., and P. A. Arkin, 1997: Global precipitation: A 17-year monthly analysis based on gauge observations, satellite estimates, and numerical model outputs. *Bull. Amer. Meteor. Soc.,* **78,** 2539–2558.

Zebiak, S. E., and M. A. Cane, 1987: A model El Niño–Southern Oscillation. *Mon Wea. Rev.,* **115,** 2262–2278.

Unauthenticated | Downloaded 02/21/24 05:03 PM UTC